ACS OMEGA

http://pubs.acs.org/journal/acsodf

Article

Inhomogeneity of Organically Modified Montmorillonite Revealed by Molecular Dynamics Simulation

Masaya Miyagawa, Fumiya Hirosawa, Hayato Higuchi, and Hiromitsu Takaba*

Cite This: *ACS Omega* 2021, 6, 19314−19322

Read Online

ACCESS | Metrics & More | Article Recommendations

ABSTRACT: The modification of an interlayer of layered materials by intercalation with an organoammonium ion has been a promising method to control the polarity of the two-dimensional nanospace. Montmorillonite is one of the best-known examples, and the modification with octadecyltrimethylammonium ion (Mont-C_{18}) results in adsorption of anthracene and pyrene together with specific excimer emission, while the nanostructure is yet to be uncovered at the molecular level because the gallery height is only ca. 27 Å. We, herein, investigated the nanostructure of this nanocomposite by molecular dynamics (MD) simulation, combined with analysis of molecular orientations against the Mont layer. The gallery height of Mont-C_{18} was well consistent with the experimental value, which was linearly increased along with the intercalation of anthracene. Anthracene was segregated on the Mont layer with its short and long molecular axes vertical in the early and late stages, respectively. In contrast, C_{18} was initially rather horizontal, forming the so-called pseudotrimolecular layer. Pushed out by anthracene, distribution and orientation of C_{18} were gradually changed: the third molecular layer was distinctly observed in the center of the interlayer in the early stage, and the orientation was changed to vertical in the late stage. Thus, the continuous increase in the gallery height is ascribed to soft response of C_{18} to the intercalation. Summarizing the abovementioned results, it was concluded that Å-order inhomogeneity is introduced in the interlayer by the intercalation of anthracene, which is significant in ideal design of the two-dimensional nanospace.

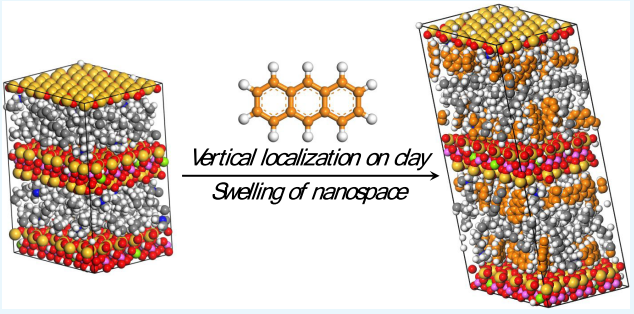

INTRODUCTION

Intercalation property of layered materials has been gaining attention in a variety of fields due to their two-dimensional interlayer space. While recovery of environmental pollutants has classically been investigated,[1−3] much effort has also been devoted to applications of catalysts, sensors, and drug delivery systems.[4−7] Some clay minerals are representative layered materials due to their natural abundance. Montmorillonite (Mont) is one of the best-known smectite-type clay minerals, whose single layer basically consists of two-dimensional Si−O tetrahedral and Al−O octahedral frameworks. Because the layers are negatively charged due to isomorphous substitution of Mg^{2+} and Fe^{2+}, exchangeable cations, typically Na^+ and K^+, are present in the interlayer for charge compensation. The intercalation of Mont is generally ascribed to the exchange of these cations and confirmed by changes in the basal spacing (sum of the height of the interlayer and thickness of the single layer) measured by powder X-ray diffraction.

The interlayer of Mont has been utilized by the intercalation of not only inorganic metal complexes,[8,9] metal cations,[10] and ionic liquids[11] but also organic molecules such as polymers,[12,13] cationic dyes,[14] and organoammonium ions,[15] the last of which endows Mont with hydrophobicity. This organically modified Mont further adsorbs nonpolar compounds such as aromatic hydrocarbon. This functionalization may seem to be derived from the hydrophobicity of the organoammonium ion, whereas the significance of interaction between the siloxane surfaces and the nonpolar compounds has been pointed out on the basis of the adsorption isotherm. In other words, the adsorbed species are assumed to be distributed inhomogeneously in the interlayer.

Spectroscopy is one of the most powerful techniques to investigate the molecular structure and its property in the interlayer. A typical example is excimer emission of anthracene (Ph_3, hereafter) and pyrene intercalated in Mont modified with octadecyltrimethylammonium ion (C_{18}).[16] Because the emission ratio of the excimer to the monomer is dependent on the preintercalated ammonium ion species, morphological control in the interlayer is significant with the aim of on-demand material design. Comprehensive understanding,

Received: June 3, 2021
Accepted: July 6, 2021
Published: July 14, 2021

however, is yet to be achieved probably because direct observation of the interlayer with a resolution of Å order is extremely difficult.

Computational chemistry is another approach to investigate the structure and the property. From a viewpoint of computational cost, molecular dynamics (MD) simulation has been extensively used rather than quantum chemical calculation. Since the late 20th century, computational methods of clays have been developed including forcefields and crystal structures.[17−23] In most cases, however, only one kind of guest species has been the subject such as polymers, organoammonium ions, ionic liquids, cationic dyes, and metal complexes.[9,24−32] In other words, the nanocomposites containing more than one guest species have hitherto been limited to relatively simple systems.[33−36] Considering the recent trend of integration with experimental studies, the development of the computational method applicable to two guest species and following understanding of the interlayer structure with the Å-order resolution will uncover fundamental strategies for the on-demand design of novel layered materials, which has ever been attempted experimentally for decades.

In the present study, we investigated the nanostructure of Ph_3-intercalated Mont modified preliminarily with C_{18} by the MD simulation. The interlayer structure of Mont modified with C_{18} (Mont-C_{18}) was well consistent with that proposed experimentally,[16] and an increase in the basal spacing of Ph_3-intercalated Mont-C_{18} (Mont-(C_{18}·Ph_3)) was also simulated, along which inhomogeneous distribution of Ph_3 in the interlayer was clearly observed. The morphologies of C_{18} and Ph_3 in the interlayer were analyzed based on atom distributions and orientation angles against the clay layer. As a result, the relation between the swelling of Mont-(C_{18}·Ph_3) and the changes in the interlayer nanostructure was revealed, which are essential to fabricate ideal two-dimensional nanoarchitecture.

Theoretical Calculations. *Outline.* Molecular dynamics simulation was performed by Forcite implemented in the Materials Studio 7.0 supplied by BIOVIA Inc. All MD simulations were conducted under a three-dimensional periodic boundary condition in a canonical ensemble (NVT) or an isothermal−isobaric ensemble (NPT). Temperature and pressure were set at 300 K and 1.0×10^{-4} GPa and controlled using the Nosé−Hoover thermostat and the Parrinello−Rahman method, respectively.[37] Dependency of the initial orientation of the Ph_3 molecule was fully removed by annealing MD with the NVT ensemble to obtain an equilibrium structure. The initial and midcycle temperatures were set at 300 and 2000 K. The heating ramps were set at 50, and the MD simulation was conducted at each step. The number of the MD simulations was 1000 per step with the time step of 1.0 fs. This annealing MD simulation was repeated 30 times. A pcff-interface developed by Heinz and co-workers was used to represent the atomic interaction,[38] which is suitable for the clay minerals to simulate the structure of the guest molecules.[23] The Lennard-Jones potential representing nonbonding atomic interactions was cut off at 10 Å with truncation correction of a cubic spline. For a summation of electrostatic interactions, the Ewald summation technique was used.[39]

Modeling of Mont-C_{18} and Mont-(C_{18}·Ph_3). A unit cell of montmorillonite composed of two pairs of a layer and an interlayer was referred to that reported previously,[40] whose parameters are a = 25.959 Å, b = 27.0459 Å, c = 20.0457 Å, α = 90.000°, β = 95.735°, and γ = 90.000°, respectively. The model formula is $Na_{0.4}[Si_4O_8][Al_{1.6}Mg_{0.4}O_2(OH)_2]$ with 108 mequiv/100 g, which is sufficiently close to that investigated experimentally.[16] The charges of the trimethylammonium (NMe_3^+) head group in C_{18} were set to −0.1 for a N atom and +0.275 for each CH_3 group, and the CH_2 group directly bonded to the N atom.[41] In the modeling of Mont-C_{18}, the unit cell was expanded to 80 Å along the c axis so as to place C_{18}. Each Na^+ ion was substituted with the cationic C_{18} with the carbon chain vertical against the clay layers. The N atoms were positioned where the deleted Na^+ ions were. After the optimization of atomic positions by molecular mechanics with 500 steps, the MD simulation was conducted with the NPT ensemble for 30 ns, which is long enough for the basal spacing to become constant, as shown in Figure 1a.

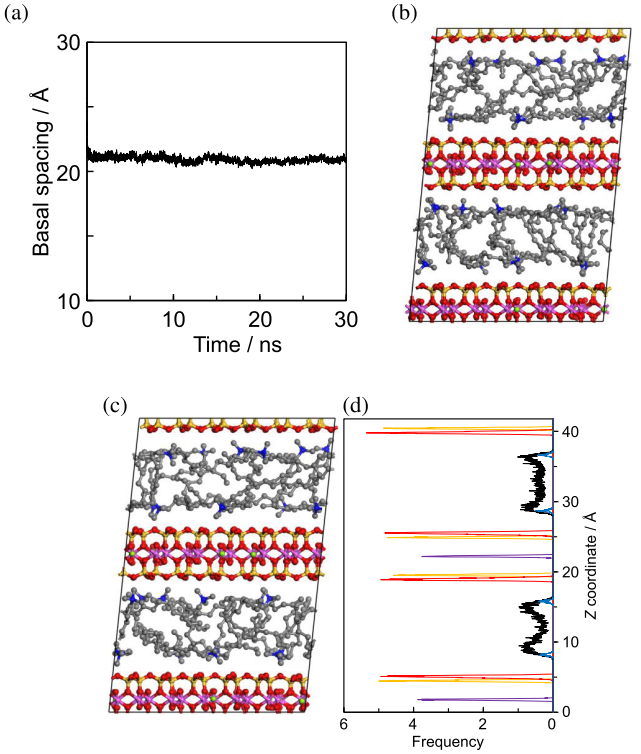

Figure 1. (a) Changes in the basal spacing of Mont-C_{18} during the MD simulation with the NPT ensemble, (b, c) snapshots of the unit cell at 25 and 30 ns, and (d) atom distributions. All of the H atoms are not displayed for clarity. The purple, green, orange, red, blue, and gray spheres in (b, c) represent Al, Mg, Si, O_{surf}, N, and C in C_{18} atoms, respectively. The colors are also corresponding to those in (d) except the C_{H2} atom, which is drawn in black.

For modeling of Mont-(C_{18}·Ph_3), the obtained Mont-C_{18} was expanded by 10 Å along the c axis. Then, the expanded structure was energetically equilibrated by performing the annealing MD followed by the MD simulation with the NVT ensemble for 5 ns. After the equilibration, five Ph_3 molecules were placed in each interlayer, whose position was further equilibrated by the same method. Finally, the expanded interlayer was shrunk by the MD simulation with the NPT ensemble for 5 ns to obtain Mont-(C_{18}·Ph_3), similar to the modeling of Mont-C_{18}. The simulation time was long enough for the basal spacing to become constant, as shown in Figure 2. Inserting the Ph_3 molecules by the abovementioned procedure repeatedly, Mont-(C_{18}·Ph_3) containing different numbers of the Ph_3 molecules was modeled.

https://doi.org/10.1021/acsomega.1c02899
ACS Omega 2021, 6, 19314−19322

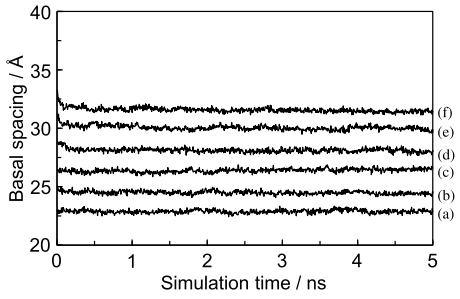

Figure 2. (a) Changes in the basal spacing of Mont-(C_{18}·Ph_3) during the MD simulation with the NPT ensemble containing (a) 5, (b) 10, (c) 15, (d) 20, (e) 25, and (f) 30 Ph_3 molecules in each interlayer, respectively.

Structural Analysis. After modeling Mont-C_{18} and Mont-(C_{18}·Ph_3), the obtained nanostructures were investigated by the MD simulation with the NVT ensemble for 5 ns. The time step was set to 1.0 fs. In the following analyses, multiple snapshots in every 100 ps were used for ensemble average.

Atom distributions of Mont-C_{18} and Mont-(C_{18}·Ph_3) were analyzed along the z axis with an interval of 0.02 Å. We note that the clay layer was set on the xy plane. Due to the two dimensionality and the swelling property, the atom distributions along the vertical z axis are significant, while those along the lateral xy directions are not. Discussing the nanostructure in the interlayer simply and definitely, we focused on the following atoms and named as denoted in the parentheses: Al atom (Al), Si atom (Si), O atom on the surface of the clay layer (O_{surf}), N atom (N), C atom in the CH_2 group of C_{18} (C_{H2}), C atom in the CH_3 tail group of C_{18} (C_{tail}), C atom in Ph_3 (C_P), and H atom in Ph_3 (H_P), respectively. The basal spacings of Mont-C_{18} and Mont-(C_{18}·Ph_3) were calculated by dividing the length of the z axis of the unit cell by two because the unit cell consists of two pairs of the layer and the interlayer.

Orientations of Ph_3 and C_{18} against the clay layer were investigated using the Cartesian coordinates of four atoms. In the Ph_3 molecule, the furthest four C atoms from the centroid were chosen and two molecular axes were defined, as shown in Figure 3a: the shorter and the longer axes are hereafter

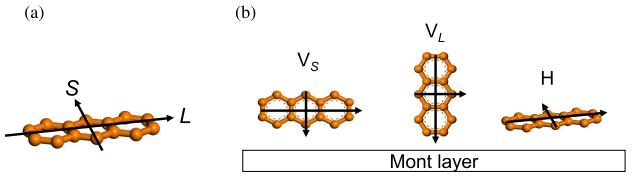

Figure 3. (a) Definition of S and L axes of Ph_3 and (b) three forms of Ph_3 with different orientations. The H atoms are not shown for clarity.

denoted as S and L, respectively. Orientation angles against the Mont layer, θ_S and θ_L, were calculated in the multiple snapshots and averaged. Here, molecular orientations are roughly divided into three groups, as shown in Figure 3b: V_S, V_L, and H forms. In the V_S form, the S and L axes are vertical and horizontal, respectively. In other words, θ_S and θ_L equal to 90 and 0°, respectively, while the opposite holds in the V_L form. In contrast, both θ_S and θ_L equal to 0° in the H form. Thus, the orientation of Ph_3 is able to be discussed by plotting θ_S against θ_L. Similarly, the orientation angle of C_{18}, θ_{C18}, was also defined using four atoms: the N atom and its nearest three C_{H2} atoms.

RESULTS AND DISCUSSION

Model Validation of Mont-C_{18}. Figure 1a shows changes in the basal spacing of Mont-C_{18} during the MD simulation with the NPT ensemble. The value is sufficiently constant after 20 ns, whose average is 20.8 Å and well consistent with the reported value, 22 Å.[16] Figure 1b,c shows the snapshots of the unit cell at 25 and 30 ns, respectively. In both snapshots, the NMe_3^+ head groups are located near the clay layers probably due to electrostatic interaction. The carbon chain of C_{18} is tangled in the interlayer, and the C_{H2} atoms are located not only horizontally near the clay layers but also in the center of the interlayer. The corresponding atom distributions are shown in Figure 1d. In each interlayer, two distinct peaks are observed in the C_{H2} atoms, which are also distributed broadly in the center of the interlayer, indicating the formation of a pseudotrimolecular layer of C_{18}, as proposed experimentally.[16] Thus, the C_{H2} atoms are found to be distributed inhomogeneously in the interlayer. Figure 4a shows a histogram of θ_{C18} in Mont-C_{18}. Based on the definition of θ_{C18}, it is found that the three C_{H2} atoms near the N atom are rather located horizontally in Mont-C_{18} because θ_{C18} is mainly distributed <15°. It is noted that similar horizontal but partially disordered nanostructures are observed theoretically in $C_{14}H_{29}N(CH_3)_3^+$ and $C_{22}H_{45}N(CH_3)_3^+$ intercalated in Mont with CEC of 145 mequiv/100 g.[32] Thus, it was concluded that Mont-C_{18} was well modeled by our MD calculations under the three-dimensional periodic boundary condition.

Nanoscopic Structure of C_{18} and Ph_3 in the Interlayer. Figure 2 shows changes in the basal spacing of Mont-(C_{18}·Ph_3) during the MD simulation with the NPT ensemble, where the Ph_3 molecules are intercalated five by five. The basal spacing is sufficiently constant during the late stage of the simulation in all of the models and is 24.4 Å in the case of 10 Ph_3 molecules, which is longer than that of Mont-C_{18}, 20.8 Å. The corresponding snapshots of the unit cell at 4 and 5 ns are shown in Figure 5a,b, respectively. Ph_3 is located on the clay layers with its S axis vertical, while the center of the interlayer seems slightly dense compared to that in Mont-C_{18}. These results are clearly confirmed by the atom distributions shown in Figure 5c. Ph_3 is found to be distributed mainly on the clay layer. In addition, the distribution of the C_{H2} atoms is not similar to that in Mont-C_{18} shown in Figure 1d: the third peak is definitely observed in the center of the interlayer, which is not in Mont-C_{18}. However, the histogram of θ_{C18} shown in Figure 4b does not change significantly compared to that in Mont-C_{18}, indicating that the orientation of the three C_{H2} atoms near the NMe_3^+ group does not change in the early stage of the intercalation of Ph_3, and the C_{H2} atoms in the middle or on the tail side of the carbon chain get partly vertically oriented. Our simulation results that C_{18} and Ph_3 are located inhomogeneously in the interlayer are actually noticeable. It is true that many experimental studies previously suggested the inhomogeneity,[15,16,42] but visualization by spectroscopy and/or microscopy is technically impossible. As far as we know, this is the first report on the visualization of the Å-order inhomogeneous interlayer induced by the intercalation of Ph_3.

As mentioned above, the C_P atoms are distributed only on the clay layer roughly with two peaks, for example around 8.5 and 10.6 Å. Hence, the orientation of Ph_3 is mainly assumed to be in the V_S form, as expected from the snapshots shown in Figure 5a,b. Figure 5d shows the corresponding orientation

https://doi.org/10.1021/acsomega.1c02899
ACS Omega 2021, 6, 19314−19322

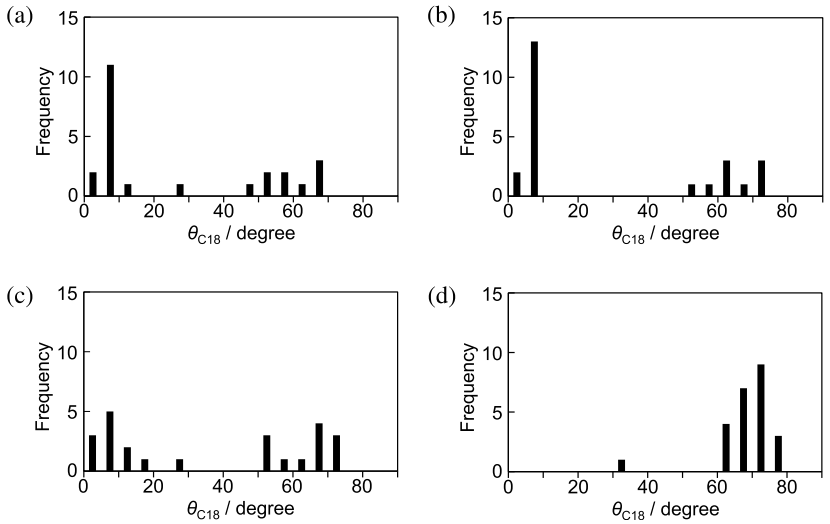

Figure 4. Histograms of θ_{C18} in (a) Mont-C_{18} and Mont-(C_{18}·Ph_3) containing (b) 10, (c) 20, and (d) 30 Ph_3 molecules in each interlayer, respectively.

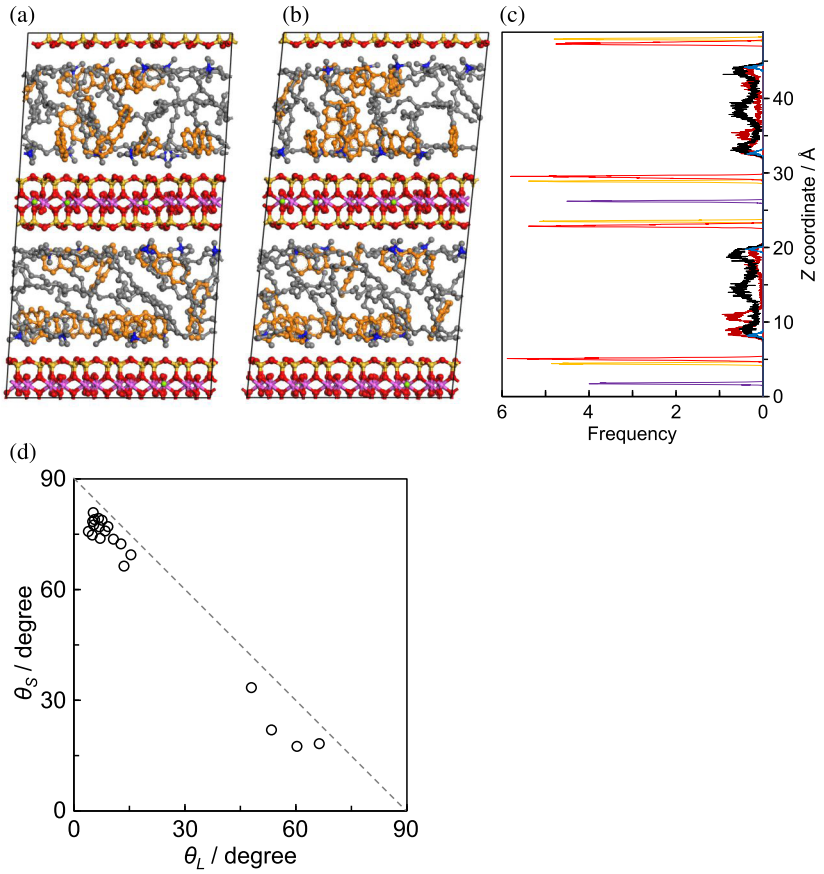

Figure 5. Snapshots of the unit cell of Mont-(C_{18}·Ph_3) containing 10 Ph_3 molecules in each interlayer at (a) 4 and (b) 5 ns, (c) atom distributions, and (d) orientation plots of Ph_3 in Mont-(C_{18}·Ph_3). The purple, green, orange, red, blue, gray, and brown spheres in (a, b) represent Al, Mg, Si, O_{surf}, N, C in C_{18}, and C_P atoms, respectively. The colors are also corresponding to those in (c) except the C_{H2} atom, which is drawn in black.

plots of the Ph_3 molecules. We note that the plots are on the broken line when the molecular plane is completely vertical to the clay layer. About 80% of the plots are located on the upper left assignable to the V_S form. The H form appearing in the lower left is not present at all. This result is rationalized by the distribution of the C_{H2} atoms shown in Figure 5c: the orientation of the C_{H2} atoms is partly vertical, resulting in the localization in the center. While the V_S and V_L forms are parallel to this locally vertical orientation of the C_{H2} atoms, the H form is not, leading to the conclusion that the H form is energetically unfavorable rather than the V_S and V_L forms.

By subtracting the thickness of the Mont layer (9.8 Å) from the basal spacing, the gallery height is calculated to be 14.6 Å, which is longer than the *L* axis, 7.3 Å. However, almost all of

https://doi.org/10.1021/acsomega.1c02899
ACS Omega 2021, 6, 19314−19322

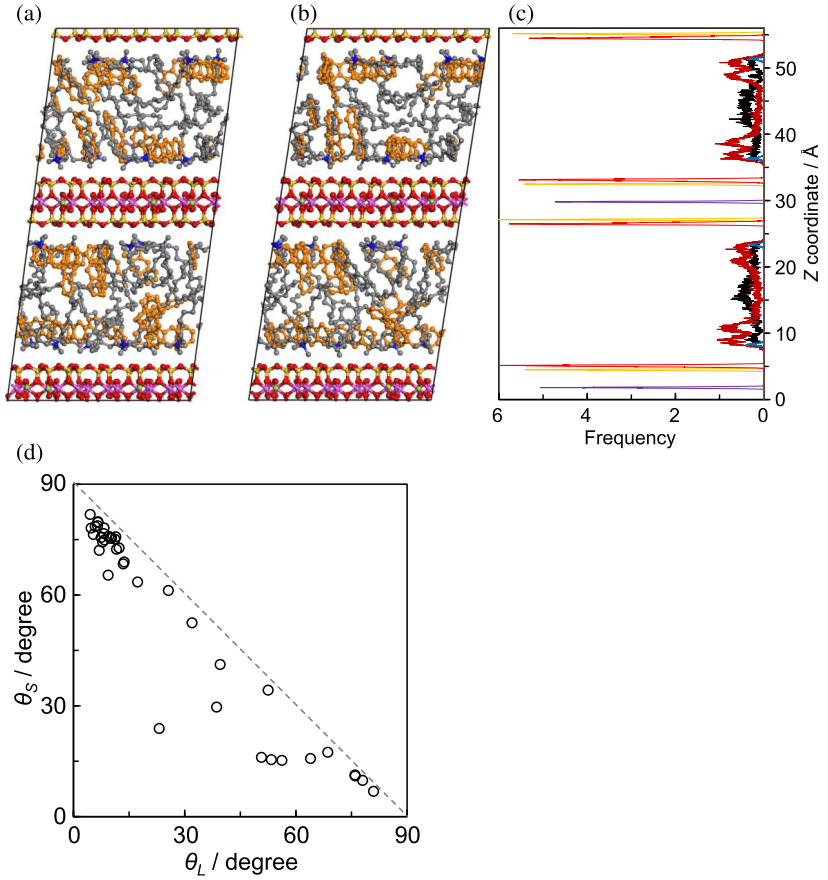

Figure 6. Snapshots of the unit cell of Mont-(C_{18}·Ph_3) containing 20 Ph_3 molecules in each interlayer at (a) 4 and (b) 5 ns, (c) atom distributions, and (d) orientation plots of Ph_3 in Mont-(C_{18}·Ph_3). The purple, green, orange, red, blue, gray, and brown spheres in (a, b) represent Al, Mg, Si, O_{surf}, N, C in C_{18}, and C_P atoms, respectively. The colors are also corresponding to those in (c) except the C_{H2} atom, which is drawn in black.

the Ph_3 molecules are present in the V_S form. This result originates from the fact that two molecular layers of Ph_3 are formed in each interlayer. It is noted that the presence of C_{18} and the H_P atoms is also not negligible. In contrast, the length of the *S* axis is 1.4 Å. Even considering the H_P atom, it is reasonable that the Ph_3 molecules are mainly present in the V_S form in the early stage of the intercalation of Ph_3, as shown in Figure 5a,b. In other words, it is suggested that the population ratio of the V_L form is possibly increased by further swelling.

Swelling-Induced Population Changes in the Orientation of Ph_3. Figure 6a,b shows the 4 and 5 ns snapshots of the unit cell of Mont-(C_{18}·Ph_3) containing 20 Ph_3 molecules in each interlayer. While Ph_3 is still localized on the clay layers in the V_S or V_L form, C_{18} seems located entirely in the interlayer. By this intercalation of Ph_3, the basal spacing is expanded to 28.0 Å. In contrast to the case of the 10 molecules, the histogram of θ_{C18} shown in Figure 4c is also changed along with the swelling: the frequency around 70° is comparable to that of around 10°, indicating that the orientation of the three C_{H2} atoms near the N atom is getting vertical.

Figure 6c shows the corresponding atom distributions. Similar to the result in the case of the 10 molecules shown in Figure 5c, the three peaks of the C_{H2} atoms are observed near the clay layers and in the center. However, the third peak in the center is fairly broadened. This broadness is corresponding to the swelling of the interlayer, which delocalizes the carbon chain of C_{18} due to an increase in the volume of the interlayer. In addition, the first peak near the clay layer is split into two at 9.04 and 9.60 Å beside the peak of the N atom. Thus, it is indicated that the nearest two C_{H2} atoms from the N atom are somewhat located vertically as supported by the histogram of θ_{C18} shown in Figure 4c.

The distribution of the C_P atoms is complementary to that of the C_{H2} atoms, and two peaks are observed near the O_{surf} atoms individually, indicating that Ph_3 is still localized on the clay layer. Figure 6d shows the orientation plots of Ph_3. In the case of 20 Ph_3 molecules, it is found that about 65% are assigned to the V_S form, while about 10% are assigned to the V_L form appearing in the lower right. Based on the above discussion in the case of 10 molecules, it is assumed that the gallery height is enough for Ph_3 to be in the V_L form. Indeed, the gallery height is calculated to be 18.2 Å, which is more than twice the length of the *L* axis. Due to the presence of C_{H2} and H_p atoms in the interlayer, Ph_3 can yet be present in the V_L form completely, leading to a rather tilted orientation plotted in the range of around 45° both in θ_S and θ_L. In addition, the first 10 Ph_3 molecules are already localized in the V_S form on the clay layers covered with the NMe_3^+ head groups. Thus, it is inferred that the V_L form becomes more energetically favorable than the V_S form for the additional 10 Ph_3 molecules in the middle stage of the intercalation.

Changes in the Orientation of C_{18} by Further Intercalation of Ph_3. Figure 7a,b shows the 4 and 5 ns snapshots of the unit cell of Mont-(C_{18}·Ph_3) containing 30 Ph_3 molecules in each interlayer. Ph_3 is located on the clay layers in

https://doi.org/10.1021/acsomega.1c02899
ACS Omega 2021, 6, 19314−19322

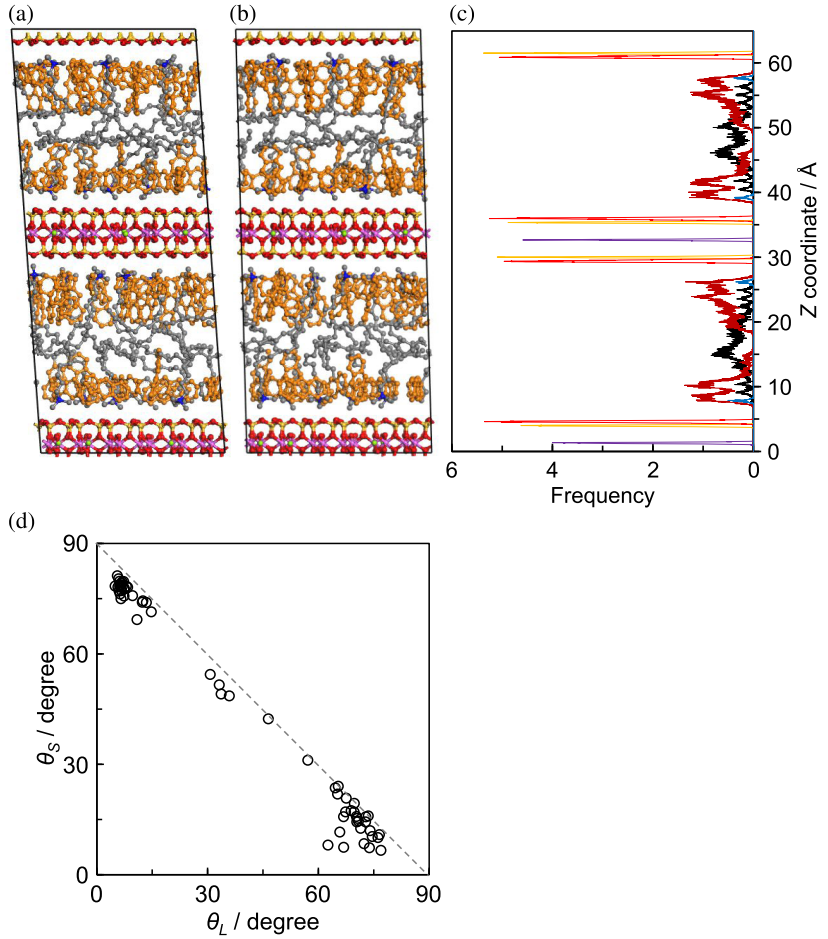

Figure 7. Snapshots of the unit cell of Mont-(C_{18}·Ph_3) containing 30 Ph_3 molecules in each interlayer at (a) 4 and (b) 5 ns, (c) atom distributions, and (d) orientation plots of Ph_3 in Mont-(C_{18}·Ph_3). The purple, green, orange, red, blue, gray, and brown spheres in (a, b) represent Al, Mg, Si, O_{surf}, N, C in C_{18}, and C_P atoms, respectively. The colors are also corresponding to those in (c) except the C_{H2} atom, which is drawn in black.

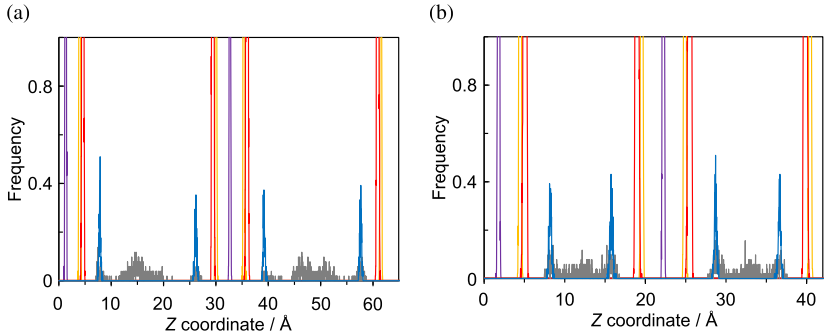

Figure 8. C_{tail} atom distributions of (a) Mont-(C_{18}·Ph_3) containing 30 Ph_3 molecules in each interlayer and (b) Mont-C_{18}, respectively. The purple, orange, red, blue, and gray lines represent Al, Si, O_{surf}, N, and C_{tail} atoms, respectively.

the V_S or V_L form, while C_{18} is stretched vertically to the clay layer. The latter result is supported by the distribution of θ_{C18}, as shown in Figure 4d. The value is mostly around 70°, and the frequency less than 30° is zero. As shown in Figure 7a,b, however, the carbon chains near the C_{tail} atoms do not seem stretched but still tangled in the center of the interlayer. This observation is supported by the distribution of the C_{tail} atoms, as shown in Figure 8a: the C_{tail} atoms are localized in the center of the interlayer in the presence of Ph_3 on the clay layers, which is in contrast to those in Mont-C_{18} shown in Figure 8b. The basal spacing is expanded to 31.4 Å, and the gallery height is calculated to be 21.6 Å, which is sufficient for the V_L form as discussed above. The orientation analysis of Ph_3 supports this assumption, as shown in Figure 7d. The ratio of the V_L form gets higher and comparable to that of the V_S form. This change is in harmony with the changes in θ_{C18} shown in Figure 4d: the vertically long V_L form is preferable when C_{18} gets vertical.

Figure 7c shows the corresponding atom distributions of Mont-(C_{18}·Ph_3). Similar to the result in the case of 20 molecules, the distribution of the C_{H2} atoms is complementary to that of the C_P atoms. In the C_P atoms, shoulder bands are

https://doi.org/10.1021/acsomega.1c02899
ACS Omega 2021, 6, 19314−19322

observed close to the center of the interlayer due to the V_L form: the C_P atoms are roughly divided into two groups in the V_S form (upper and lower halves), while located rather homogeneously in the V_L form. Contrary to the case of 20 molecules, the broad peak in the center of the interlayer is split into two. This split originates from the continuous expansion of the interlayer by the intercalation of Ph_3. Moreover, not two but three sharp peaks of the C_{H2} atoms are observed beside each N atom, assignable to the three C_{H2} atoms near the N atom used for θ_{C18}. Distances between two adjacent peaks are 1.32, 1.24, and 1.21 Å for N−C, C−C, and C−C respectively. When the molecular axis of C_{18} is completely vertical to the clay layer, the distances are 1.37 and 1.26 Å for N−C and C−C, respectively. Therefore, it was concluded that the three C_{H2} atoms near the N atom are oriented almost vertically to the clay layer. This result is consistent with the snapshots and θ_{C18} shown in Figures 7a,b, and 4d, respectively.

Dynamics of Swelling and Structural Characteristics. Figure 9 shows the correlation between the basal spacing of the

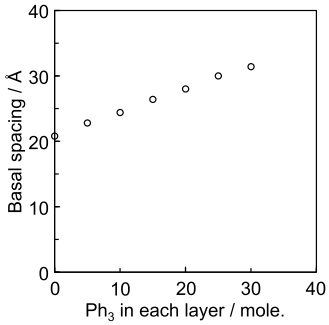

Figure 9. Correlation between the basal spacing and the number of the Ph_3 molecules in each interlayer.

nanocomposite and the number of Ph_3 in each interlayer. The swelling takes place continuously by the intercalation. It is true that the swelling seems to originate from the increase in the volume due to Ph_3, but the nanostructural behavior is actually not simple. First, the C_{H2} atoms are distributed mainly near the clay layers to form the pseudotrimolecular layer in Mont-C_{18}, as shown in Figure 1d. Second, the third layer of the C_{H2} atoms becomes distinctly observed in the center by the intercalation of 10 Ph_3 molecules, as shown in Figure 5c. In this nanocomposite, the swelling is ascribed to the fact that Ph_3 is localized on the clay layers and pushed out the C_{H2} atoms in the middle or on the tail side of the carbon chain, whereas the three C_{H2} atoms near the N atom are still mainly horizontal, resulting in the three peaks in the distribution of the C_{H2} atoms. However, the expanded gallery height is not sufficient for Ph_3 to be present in the V_L form. Consequently, the V_S form is dominant. Third, further swelling takes place by the intercalation of Ph_3, along which the C_{H2} atoms near the N atom get oriented vertically, as shown in Figures 4c and 6c. This swelling enables the additional Ph_3 molecules on the clay layer to be present in the V_L form. Finally, C_{18} gets vertical almost completely and the ratio of the V_L form is increased, as shown in Figures 4d and 7d. Therefore, the swelling in the late stage is ascribed to the changes of θ_{C18}, whose distribution is shown in Figure 4. In other words, the flexibility of C_{18} enables the interlayer of Mont to swell smoothly and determines the basal spacing.

Population changes in the V_S and V_L forms against the number of the Ph_3 molecules are summarized in Figure 10. It is

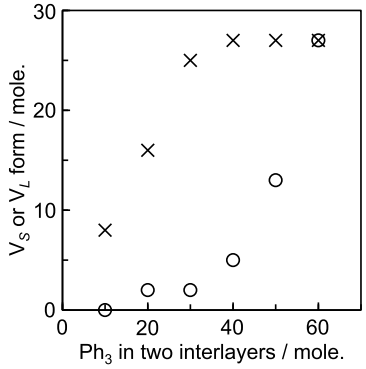

Figure 10. Population changes of the V_S and V_L forms against the number of the Ph_3 molecules. The marks × and ○ represent the V_S and V_L forms, respectively. In this analysis, the V_S and V_L forms are defined when $\theta_S > 60°$ and $\theta_L < 30°$ in V_S, and $\theta_S < 30°$ and $\theta_L > 60°$ in V_L, respectively.

clearly demonstrated that the V_S form is dominant in the early stage but saturated in the middle stage, while the V_L form is drastically increased correspondingly. We assume that the increase in the population of the V_L form in the middle and late stages is ascribed to the coverage of the clay layers with the NMe_3^+ head groups and Ph_3 in the V_S form. In the MD simulation, the orientation changes from the V_S to V_L form did not take place, suggesting that the V_S form is favorably interacted with the clay layer strongly compared to the V_L form. Based on the number of the H_P atoms in Ph_3 faced to the clay layer, it is convincing that the Ph_3 molecules in the V_S form are more stabilized than those in the V_L form. Our result of the localization of Ph_3 on the clay layers is consistent with that reported previously.[15] It was experimentally suggested that the clay layers play a significant role in the adsorption of aromatic hydrocarbons. The localization of Ph_3 also possibly rationalizes the excimer emission of Ph_3 in Mont-(C_{18}·Ph_3).[16] As shown in Figure 7a,b, the Ph_3 molecules are parallel to each other, which is necessary for the formation of the excimer.

Because the length of C_{18} is approximately consistent with the gallery height of Mont-(C_{18}·Ph_3),[16] one may think that the carbon chain is stretched thoroughly at the saturated adsorption state. However, it is highly improbable due to the coverage of the clay layers with the NMe_3^+ head groups and Ph_3 molecules. The atom distributions of the C_{tail} atoms shown in Figure 8 support our assumption. The C_{tail} atoms are originally located both on the clay surface and in the center of the interlayer in Mont-C_{18}. By the intercalation of 30 Ph_3 molecules, the distribution is changed and localized in the center. Combined with the changes in θ_{C18} shown in Figure 4, it is found that the three C_{H2} atoms near the N atom are oriented vertically, while the C_{H2} atoms in the other part of the chain are relatively flexible, leading to the localization of the C_{tail} atom in the center of the interlayer, as shown in Figure 7a,b. Therefore, nanoscopic segregations of C_{18} and Ph_3 were revealed by the MD simulation and following structural analyses.

CONCLUSIONS

In the present study, we investigated the nanostructure of Mont-(C_{18}·Ph_3) by MD simulation combined with the

https://doi.org/10.1021/acsomega.1c02899
ACS Omega 2021, 6, 19314−19322

analyses of the vertical atom distributions and the orientation angles of C_{18} and Ph_3. Stepwise intercalation of Ph_3 revealed that the increase in the basal spacing is continuous, which cannot be realized easily by an experiment. The Ph_3 molecules are localized in the V_S or V_L form on the Mont layers. By the intercalation of Ph_3, the orientation of C_{18} is changed gradually from horizontal to vertical. Thus, the swelling of the interlayer is ascribed not to the volume of the Ph_3 molecules but to the orientation changes in C_{18}. Summarizing the changes in the distribution of the C_{H2}, C_{tail}, and C_P atoms, it was concluded that the Ph_3 molecules are distributed in the interlayer inhomogeneously, whereas such segregation possibly induces the characteristic photophysical behavior. We believe that our results demonstrate the significance of the flexibility of C_{18} and give an insight into the on-demand material design.

AUTHOR INFORMATION

Corresponding Author

Hiromitsu Takaba − *Department of Environmental Chemistry & Chemical Engineering, School of Advanced Engineering, Kogakuin University, Hachioji, Tokyo 192-0015, Japan*; Email: takaba@cc.kogakuin.ac.jp

Authors

Masaya Miyagawa − *Department of Environmental Chemistry & Chemical Engineering, School of Advanced Engineering, Kogakuin University, Hachioji, Tokyo 192-0015, Japan*; orcid.org/0000-0002-3141-9440

Fumiya Hirosawa − *Department of Environmental Chemistry & Chemical Engineering, School of Advanced Engineering, Kogakuin University, Hachioji, Tokyo 192-0015, Japan*

Hayato Higuchi − *Department of Environmental Chemistry & Chemical Engineering, School of Advanced Engineering, Kogakuin University, Hachioji, Tokyo 192-0015, Japan*

Complete contact information is available at: https://pubs.acs.org/10.1021/acsomega.1c02899

Author Contributions

This manuscript was written through the contributions of all authors. All authors have given approval to the final version of the manuscript.

Notes

The authors declare no competing financial interest.

ACKNOWLEDGMENTS

The authors appreciate support from JSPS KAKENHI Grant Number 21K14705.

REFERENCES

(1) Zubair, M.; Daud, M.; McKay, G.; Shehzad, F.; Al-Harthi, M. A. Recent progress in layered double hydroxides (LDH)-containing hybrids as adsorbents for water remediation. *Appl. Clay Sci.* **2017**, *143*, 279−292.

(2) Celis, R.; Hermosín, M. C.; Cornejo, J. Heavy Metal Adsorption by Functionalized Clays. *Environ. Sci. Technol.* **2000**, *34*, 4593−4599.

(3) Pazos, M. C.; Bravo, L. R.; Ramos, S. E.; Osuna, F. J.; Pavón, E.; Alba, M. D. Multiple pollutants removal by functionalized heterostructures based on Na-2-Mica. *Appl. Clay Sci.* **2020**, *196*, No. 105749.

(4) Bodhankar, P. M.; Sarawade, P. B.; Singh, G.; Vinu, A.; Dhawale, D. S. Recent advances in highly active nanostructured NiFe LDH catalyst for electrochemical water splitting. *J. Mater. Chem. A* **2021**, *9*, 3180−3208.

(5) Tominaga, M.; Oniki, Y.; Mochida, S.; Kasatani, K.; Tani, S.; Suzuki, Y.; Kawamata, J. Clay-Organic Hybrid Films Exhibiting Reversible Fluorescent Color Switching Induced by Swelling and Drying of a Clay Mineral. *J. Phys. Chem. C* **2016**, *120*, 23813−23822.

(6) Esmat, M.; Farghali, A. A.; El-Dek, S. I.; Khedr, M. H.; Yamauchi, Y.; Bando, Y.; Fukata, N.; Ide, Y. Conversion of a 2D Lepidocrocite-Type Layered Titanate into Its 1D Nanowire Form with Enhancement of Cation Exchange and Photocatalytic Performance. *Inorg. Chem.* **2019**, *58*, 7989.

(7) Yan, L.; Gonca, S.; Zhu, G.; Zhang, W.; Chen, X. Layered double hydroxide nanostructures and nanocomposites for biomedical applications. *J. Mater. Chem. B* **2019**, *7*, 5583−5601.

(8) Sato, H.; Takimoto, K.; Kato, M.; Nagaoka, S.; Tamura, K.; Yamagishi, A. Real-Time Monitoring of Low Pressure Oxygen Molecules over Wide Temperature Range: Feasibility of Ultrathin Hybrid Films of Iridium(II) Complexes and Clay Nanosheets. *Bull. Chem. Soc. Jpn.* **2020**, *93*, 194−199.

(9) Sainz-Díaz, C. I.; Bernini, F.; Castellini, E.; Malferrari, D.; Borsari, M.; Mucci, A.; Brigatti, M. F. Experimental and Theoretical Investigation of Intercalation and Molecular Structure of Organo-Iron Complexes in Montmorillonite. *J. Phys. Chem. C* **2018**, *122*, 25422−25432.

(10) Chen, C.; Liu, H.; Chen, T.; Chen, D.; Frost, R. L. An Insight into the removal of Ph(II), Cu(II), Co(II), Cd(II), Zn(II), Ag(I), Hg(I), Cr(VI) by Na(I)-montmorillonite and Ca(II)-montmorillonite. *Appl. Clay Sci.* **2015**, *118*, 239−247.

(11) Naderi, A.; Delavar, M. A.; Ghorbani, Y.; Kaboudin, B.; Hosseini, M. Modification of nano-clays with ionic liquids for the removal of Cd(II) ion from aqueous phase. *Appl. Clay Sci.* **2018**, *158*, 236.

(12) Tyan, H.-L.; Leu, C.-M.; Wei, K.-H. Effect of Reactivity of Organics-Modified Montmorillonite on the Thermal and Mechanical Properties of Montmorillonite/Polyimide Nanocomposites. *Chem. Mater.* **2001**, *13*, 222−226.

(13) Usuki, A.; Kojima, Y.; Kawasumi, M.; Okada, A.; Fukushima, Y.; Kurauchi, T.; Kamigaito, O. Synthesis of nylon 6-clay hybrid. *J. Mater. Res.* **1993**, *8*, 1179−1184.

(14) Takagi, S.; Shimada, T.; Masui, D.; Tachibana, H.; Ishida, Y.; Tryk, D. A.; Inoue, H. Unique Solvatochromism of a Membrane Composed of a Cationic Porphyrin-Clay Complex. *Langmuir* **2010**, *26*, 4639−4641.

(15) Jaynes, W. F.; Boyd, S. A. Hydrophobicity of Siloxane Surfaces in Smectites as Revealed by Aromatic Hydrocarbon Adsorption from Water. *Clays Clay Miner.* **1991**, *39*, 428−436.

(16) Ogawa, M.; Aono, T.; Kuroda, K.; Kato, C. Photophysical Probe Study of Alkylammonium-Montmorillonites. *Langmuir* **1993**, *9*, 1529−1533.

(17) Delville, A. Modeling of the Clay-Water Interface. *Langmuir* **1991**, *7*, 547−555.

(18) Collins, D. R.; Catlow, C. R. A. Computer simulation of structures and cohesive properties of micas. *Am. Mineral.* **1992**, *77*, 1172−1181.

(19) Dove, M. T.; Heine, V. The use of Monte Carlo methods to determine the distribution of Al and Si cations in framework aluminosilicates from ^{29}Si MAS NMR data. *Am. Mineral.* **1996**, *81*, 39−44.

(20) Sainz-Díaz, C. I.; Hernández-Laguna, A.; Dove, M. T. Phys. Chem. Miner. Modeling of dioctahedral 2:1 phyllosilicates by means of transferable empirical potentials. *Phys. Chem. Miner.* **2001**, *28*, 130−141.

(21) Sainz-Díaz, C. I.; Palin, E. J.; Dove, M. T.; Hernández-Laguna, A. Monte Carlo simulations of ordering of Al, Fe, and Mg cations in the octahedral sheet of smectites and illites. *Am. Mineral.* **2003**, *88*, 1033−1045.

(22) Cygan, R. T.; Liang, J.-J.; Kalinichev, A. G. Molecular Models of Hydroxide, Oxyhydroxide, and Clay Phases and the Development of a General Force Field. *J. Phys. Chem. B* **2004**, *108*, 1255−1266.

(23) Heinz, H.; Koerner, H.; Anderson, K. L.; Vaia, R. A.; Farmer, B. L. Force Field of Mica-Type Silicates and Dynamics of Octadecy-

lammonium Chains Grafted to Montmorillonite. *Chem. Mater.* **2005**, *17*, 5658−5669.
(24) Gaudel-Siri, A.; Brocorens, P.; Siri, D.; Gardebien, F.; Brédas, J.-L.; Lazzaroni, R. Molecular Dynamics Study of ε-Caprolactone Intercalated in Wyoming Sodium Montmorillonite. *Langmuir* **2003**, *19*, 8287−8291.
(25) Pospíšil, M.; Čapková, P.; Weissmannová, H.; Klika, Z.; Trchová, M.; Chmielová, M.; Weiss, Z. Structure analysis of montmorillonite intercalated with rhodamine B: modeling and experiment. *J. Mol. Model.* **2003**, *9*, 39−46.
(26) Gardebien, F.; Brédas, J.-L.; Lazzaroni, R. Molecular Dynamics Simulations of Nanocomposites Based on Poly(ε-caprolactone) Grafted on Montmorillonite Clay. *J. Phys. Chem. B* **2005**, *109*, 12287−12296.
(27) Sikdar, D.; Katti, D. R.; Katti, K. S. A Molecular Model for ε-Caprolactam-Based Intercalated Polymer Clay Nanocomposite: Integrating Modeling and Experiments. *Langmuir* **2006**, *22*, 7738−7747.
(28) Mazo, M. A.; Manevitch, L. I.; Gusarova, E. B.; Shamaev, M. Y.; Berlin, A. A.; Baalabaev, N. K.; Rutledge, G. C. Molecular Dynamics Simulation of Thermomechanical Properties of Montmorillonite Crystal. 3. Montmorillonite Crystals with PEO Oligomer Intercalates. *J. Phys. Chem. B* **2008**, *112*, 3597−3604.
(29) Zhao, Q.; Burns, S. E. Microstructure of Single Chain Quaternary Ammonium Cations Intercalated into Montmorillonite: A Molecular Dynamics Study. *Langmuir* **2012**, *28*, 16393−16400.
(30) Wu, L.; Yang, C.; Mei, L.; Qin, F.; Liao, L.; Lv, G. Microstructure of different chain length ionic liquids intercalated into montmorillonite: A molecular dynamics study. *Appl. Clay Sci.* **2014**, *99*, 266−274.
(31) Camara, M.; Liao, H.; Xu, J.; Zhang, J.; Swai, R. Molecular dynamics study of the intercalation and conformational transition of poly(N-vinyl caprolactam), a thermosensitive polymer in hydrated Na-montmorillonite. *Polymer* **2019**, *179*, No. 121718.
(32) Heinz, H.; Vaia, R. A.; Krishnamoorti, R.; Farmer, B. L. Self-Assembly of Alkylammonium Chain on Montmorillonite: Effect of Chain Length, Head Group Structure, and Cation Exchange Capacity. *Chem. Mater.* **2007**, *19*, 59−68.
(33) Krishnan, M.; Saharay, M.; Kirkpatrick, R. J. Molecular Dynamics Modeling of CO_2 and Poly(ethylene glycol) in Montmorillonite: The Structure of Clay-Polymer Composites and the Incorporation of CO_2. *J. Phys. Chem. C* **2013**, *117*, 20592−20609.
(34) Myshakin, E. M.; Saidi, W. A.; Romanov, V. N.; Cygan, R. T.; Jordan, K. D. Molecular Dynamics Simulations of Carbon Dioxide Intercalation in Hydrated Na-Montmorillonite. *J. Phys. Chem. C* **2013**, *117*, 11028−11039.
(35) Sena, M. M.; Morrow, C. P.; Kirkpatrick, R. J.; Marimuthu, K. Supercritical Carbon Dioxide at Smectite Mineral-Water Interfaces: Molecular Dynamics and Adaptive Biasing Force Investigation of CO_2/H_2O Mixtures Nanoconfined in Na-Montmorillonite. *Chem. Mater.* **2015**, *27*, 6946−6959.
(36) Sakuma, H.; Tamura, K.; Hashi, K.; Kamon, M. Caffeine Adsorption on Natural and Synthetic Smectite Clays: Adsorption Mechanism and Effect of Interlayer Cation Valence. *J. Phys. Chem. C* **2020**, *124*, 25369−25381.
(37) Martyna, G. J.; Tobias, J. T.; Klein, M. L. Constant pressure molecular dynamics algorithms. *J. Chem. Phys.* **1994**, *101*, 4177−4189.
(38) Heinz, H.; Lin, T.-J.; Mishra, R. K.; Emami, F. S. Thermodynamically Consistent Force Field for the Assembly of Inorganic, Organic, and Biological Nanostructures: The INTERFACE Force Field. *Langmuir* **2013**, *29*, 1754−1765.
(39) Ewald, P. P. Die Berechnung optischer und elektrostatischer Gitterpotentiale. *Ann. Phys.* **1921**, *369*, 253.
(40) Heinz, H.; Suter, U. W. Surface Structure of Organoclays. *Angew. Chem., Int. Ed.* **2004**, *43*, 2239−2243.
(41) Heinz, H.; Suter, U. W. Atomic Charges for Classical Simulations of Polar Systems. *J. Phys. Chem. B* **2004**, *108*, 18341−18352.
(42) Okada, T.; Ogawa, M. Adsorption of Phenol onto 1,1′-Dimethyl-4,4′-bipyridinium-smectites. *Chem. Lett.* **2002**, *31*, 812−813.

https://doi.org/10.1021/acsomega.1c02899
ACS Omega 2021, 6, 19314−19322